

The evolutionary stage of Betelgeuse inferred from its pulsation periods

Hideyuki Saio,^{1*} Devesh Nandal,² Georges Meynet² and Sylvia Ekstöm²

¹*Astronomical Institute, Graduate School of Science, Tohoku University, Aramaki, Aoba-ku, Sendai, Miyagi, 980-8578, Japan*

²*Département d'Astronomie, Université de Genève, Chemin Pegasi 51, CH-1290 Versoix, Switzerland*

Accepted XXX. Received YYY; in original form ZZZ

ABSTRACT

Betelgeuse is a well known bright red supergiant that shows semi-regular variations with four approximate periods of 2200, 420, 230, and 185 days. While the longest period was customarily regarded as LSP (long secondary period) of unknown origin, we identify the ~ 2200 -d period as the radial fundamental mode, and the three shorter periods as the radial first, second, and third overtones. From a linear nonadiabatic pulsation analysis including the pulsation/convection coupling, we have found that these radial pulsation modes are all excited in the envelope of a model in a late stage of the core-carbon burning. Models with similar pulsation property have masses of $11 \sim 12 M_{\odot}$ ($19 M_{\odot}$ at ZAMS) with luminosities ($\log L/L_{\odot} = 5.27 \sim 5.28$) and effective temperatures ($\log T_{\text{eff}} \approx 3.53$) that are consistent with the range of the observational determinations. We also find that a synthetic light curve obtained by adding the fundamental and the first-overtone mode is comparable with the light curve of Betelgeuse up to the Great Dimming. We conclude that Betelgeuse is likely in the late stage of core carbon burning, and a good candidate for the next Galactic Type II supernova.

Key words: stars: evolution – stars: massive – stars: oscillations – stars: individual: Betelgeuse (α Ori)

1 INTRODUCTION

Betelgeuse (α Orionis; HD 39801) is a nearby luminous red supergiant (RSG; M1-2 Iab-a) located approximately 200 parsec from the Sun, has a fascinating past. For example, from investigating of pre-telescopic records Neuhäuser et al. (2022) found that its surface temperature was significantly higher two millennia ago. Betelgeuse shows semi-periodic light variations, which have been observed for more than a century (AAVSO¹). These and other very interesting phenomena that occurred in and around Betelgeuse are nicely reviewed in Wheeler & Chatzopoulos (2023).

The brightness of Betelgeuse decreased abnormally (called ‘Great Dimming’) from December 2019 to February 2020 (by ~ 1.2 mag) around a minimum epoch of ~ 400 d variation (Guinan et al. 2019). Stimulated by the mysterious dimming, many intensive observations in various wavelengths, and detailed analyses have been carried out. These investigations suggest that effective temperature decreased by ~ 100 K (e.g., Dharmawardena et al. 2020; Harper et al. 2020; Taniguchi et al. 2022; Wasatonic 2022; Mittag et al. 2023) during the Great Dimming, and a substantial mass ejection possibly occurred (e.g., Montargès et al. 2021; Kravchenko et al. 2021; Taniguchi et al. 2022; Dupree et al. 2022; Jadlovský et al. 2023).

Given Betelgeuse’s high luminosity and its complex variations, which could potentially indicate an impending supernova event, the evolution of this star has been the subject of numerous investigations (e.g., Meynet et al. 2013; Dolan et al. 2016; Wheeler et al. 2017; Nance et al. 2018; Luo et al. 2022). Its high rotation rate $v_{\text{eq}} = 6.5^{+4.1}_{-0.8}$ km s⁻¹ (Kervella et al. 2018) as a red supergiant has

stimulated discussions on the evolution involving merger with a past companion (Sullivan et al. 2020) as a source of angular momentum.

Pulsation periods of the semi-regular variations of Betelgeuse are very useful to constrain its present fundamental parameters and the evolution stage. Periods of 2200 d and 420 d are obvious and most frequently mentioned. So far, the 420-d period was customarily considered to be the radial fundamental mode (e.g. Joyce et al. 2020), and the 2200-d period to be a LSP (Long Secondary Period) caused by something other than radial pulsations. However, we will show, in this paper, that in a luminous supergiant like Betelgeuse long-period pulsations are very nonadiabatic so that 2200-d period is suitable for the radial fundamental mode, and the 420-d period should be identified as the first overtone mode. We can confirm this mode identifications by extending the period-luminosity (PL) relations of less luminous red-giant (RG) to the RSG range in Fig.7 of Kiss et al. (2006) (or Fig.6 of Chatys et al. 2019). We find that the 420-d period at $M_{\text{K}} \approx -10$ mag (M_{K} = absolute magnitude in K band) lies on the extension of sequence B which is identified as the first overtone radial pulsation (e.g., Trabucchi et al. 2017). This clearly indicates the 420-d period to be the first overtone mode of Betelgeuse. Since the pulsation period of a given mode is shorter for a smaller radius, the size of Betelgeuse would be significantly underestimated if the 420-d period were fitted with radial fundamental mode (rather than first overtone).

2 OBSERVATIONAL CONSTRAINTS

2.1 Global parameters

Lobel & Dupree (2000) obtained the surface gravity $\log g = -0.5$ and effective temperature $T_{\text{eff}} = 3500 \pm 100$ K by fitting of synthetic

* E-mail: saio@astr.tohoku.ac.jp (HS)

¹ The AAVSO International Database, <https://www.aavso.org>

profiles to unblended metal absorption lines in the near-IR spectra. Furthermore, from CO equivalent widths for Betelgeuse Carr et al. (2000) obtained $T_{\text{eff}} = 3540 \pm 260$ K. More recently, Levesque & Massey (2020) obtained $T_{\text{eff}} = 3600 \pm 25$ K from optical spectrophotometry. Based on these spectroscopic T_{eff} determinations for Betelgeuse, we adopt $T_{\text{eff}} = 3500 \pm 200$ K for a constraint for our models, and note that the T_{eff} range is the same as that adopted by Dolan et al. (2016).

As emphasized in Josselin et al. (2000), K-magnitude is more useful in deriving bolometric luminosity of Red supergiants (RSG) rather than V-magnitude, because the K-bolometric correction is insensitive to the effective temperature and surface gravity. In addition, K-magnitude is less affected by interstellar extinction or pulsation. From the 2MASS All-Sky Catalog of Point Sources (Cutri et al. 2003), K-magnitude of Betelgeuse is -4.378 ± 0.186 mag. Adopting the distance of 222^{+48}_{-34} pc from the new combined radio+Hipparcos astrometric solution obtained by Harper et al. (2017), and K-bolometric correction 2.92 ± 0.16 (Levesque et al. 2005) for $T_{\text{eff}} = 3500 \pm 200$ K, we obtain $\log L/L_{\odot} = 5.18 \pm 0.11$ for Betelgeuse (which is similar to 5.10 ± 0.22 adopted by Dolan et al. 2016).

2.2 Observed pulsation periods

The semi-regular light variations of Betelgeuse indicate several periodicities ranging from ~ 2200 d to 185 d to be simultaneously excited. Indeed, every period analysis for Betelgeuse light curve yielded more than two periods (Jadlovský et al. 2023; Ogane et al. 2022; Wasatonic 2022; Granzer et al. 2022; Joyce et al. 2020; Kiss et al. 2006; Stothers & Leung 1971). Table 1 lists most recent period determinations by various authors. Among five groups of periods, we have selected the four periods P_1, P_2, P_3 and P_4 as listed in the last line of Table 1. (The 365-day period of Jadlovský et al. (2023) is considered to be one year alias.) Regarding these four periods being caused by radial pulsations of Betelgeuse, we have searched for evolution models which simultaneously excite pulsations of the four periods P_1, \dots, P_4 in the range of the error box for Betelgeuse in the HR diagram.

3 MODELS

Evolution models of massive stars from ZAMS (Zero-age main-sequence) up to the end of core-carbon burning (to the end of silicon burning for a selected case) have been computed using the recent version of the Geneva stellar evolution code (GENEC: Ekström et al. 2012; Yusof et al. 2022). We have assumed the same initial chemical composition of Yusof et al. (2022); i.e., initial mass fractions of hydrogen and heavy elements are set as $X = 0.706, Z = 0.020$. The mixing length to pressure scale height is set 1.6 for the envelope convection. Convective core boundaries are determined using the Schwarzschild criterion with a step overshooting of $0.1 H_p$ with H_p being the pressure scale height at the boundary.

We adopt initial rotation velocities, v_i of 0.1, 0.2, or $0.4 v_{\text{crit}}$ with v_{crit} being the critical rotation velocity at ZAMS. While the resulted rotation velocities in the envelopes of the red supergiants are too small to impact the radial pulsations, rotational mixing increases effective core mass and hence luminosity (Ekström et al. 2012; Yusof et al. 2022). Furthermore, CNO abundances at the surface are affected by the assumed initial rotation rates.

We have obtained periods and stability (i.e., excitation/damping) of radial pulsations of various models using the same nonadiabatic linear radial pulsation code employed in Anderson et al. (2016) for Cepheid pulsations. The pulsation code is based on that described

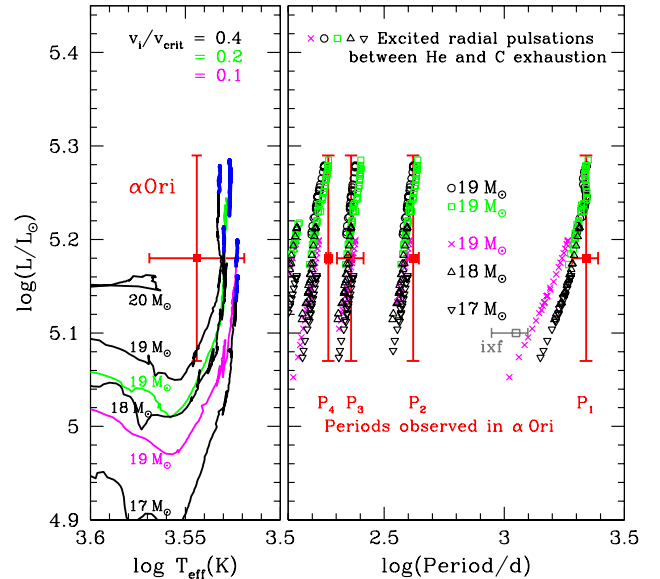


Figure 1. **Left panel:** The location of Betelgeuse (α Ori) and various evolutionary tracks on the HR diagram. The blue-coloured sections represent the phase of core-carbon burning. The number along each track indicates the initial mass in solar units. The $20 M_{\odot}$ -track is taken from Yusof et al. (2022). **Right panel:** Period-luminosity diagram showing observed four periods of Betelgeuse with error bars (red lines), and various symbols for excited radial-pulsation periods along the evolutionary tracks from the He exhaustion to the Carbon exhaustion at the stellar center. For comparison, the pulsation period of the RSG progenitor of SN2023ixf (in M101) obtained by Jencson et al. (2023) is shown by the gray horizontal bar labelled as "ixf".

in Saio et al. (1983) but revised to include the effect of the coupling between pulsation and time-dependent convection. As summarized in Sec.2.2 of Anderson et al. (2016), the convection effects are included based on the works by Unno (1967) and Grigahcène et al. (2005), which successfully predicts the red-edge of the cepheid instability strip. Details of the pulsation code are discussed in Appendix A.

4 RESULTS

4.1 Periods of excited radial pulsations

We have applied our non-adiabatic radial pulsation code to selected evolution models which enter the error box on the HR diagram (Figure 1). We have found that the four radial pulsation modes having periods similar to those observed in Betelgeuse (right panel of Fig. 1) are excited in models located in the cooler and luminous part of the error box in the HR diagram as shown in Figure 1. Table 2 lists good models in which all the excited radial pulsation periods agree with the observed four periods. These models are in the carbon-burning (or ending) phase having luminosities in the range of $5.26 < \log L/L_{\odot} < 5.28$. The mass at ZAMS was $19 M_{\odot}$ and has been reduced to $\sim 11 - 12 M_{\odot}$ at the phase of Betelgeuse.

Note that we need a high luminosity in the upper range of error bar, because the predicted period of the third overtone mode deviates from P_4 quickly as the luminosity decreases, while P_1 varies slowly as seen in the right panel of Figure 1. This property of P_4 sets the lowest luminosity acceptable among models with $v_i = 0.2 v_{\text{crit}}$ at

Table 1. Recent period determinations for light and radial-velocity curves of Betelgeuse and the adopted periods in this paper

Authors	Periods (d)					Data
Jadlovský et al. (2023):	2190 ± 270	417 ± 17	365 ± 75	230 ± 29	185 ± 4	AAVSO ¹⁾ ,SMEI ²⁾
Ogane et al. (2022):	2160	405		202 ^{a)}		UBVRI photometry
Wasatonic (2022):	2209 ± 183	439 ± 5				V & NIR photometry
Granzer et al. (2022):	2169 ± 6.3	394.5		216.0		STELLA ³⁾
Joyce et al. (2020):	2365 ± 10	416 ± 24			185.5 ± 0.1	AAVSO,SMEI
Kiss et al. (2006):	2050 ± 460	388 ± 30				AAVSO
Adopted in this work:	P_1 2190 ± 270	P_2 417 ± 24		P_3 230 ± 29	P_4 185 ± 4	

¹⁾ AAVSO= American Association Variable Star Observers, ²⁾ SMEI= Solar Mass Ejection Imager ³⁾ STELLA= échelle spectrograph
^{a)} If this periodicity is subtracted from the V-band data as the harmonic of 405 d, additional periods of 237.7 d and 185.8 d are obtained.

Table 2. Model examples which excite pulsations consistent with periods of Betelgeuse

Model	$M_i^a)$	v_i/v_{crit}	P_1 [d]	P_2 [d]	P_3 [d]	P_4 [d]	$M^a)$	$\log L/L_\odot$	$\log T_{\text{eff}}[K]$	$\log R/R_\odot$	$X_c(C)^b)$
α Ori			2190 ± 270	417 ± 24	230 ± 29	185 ± 4		5.18 ± 0.11	3.544 ± 0.025		
A	19	0.4	2199	418	240	178	11.23	5.279	3.532	3.100	0.0067
B	19	0.2	2186	434	252	184	11.73	5.276	3.526	3.109	0.0048
C	19	0.2	2181	434	252	184	11.73	5.275	3.526	3.109	0.0503
D	19	0.2	2168	428	249	181	11.73	5.265	3.526	3.103	0.1712

^{a)} Initial mass M_i and present mass M in the solar unit.

^{b)} Mass fraction of carbon at the center.

model D (Table 2) which has $\log L/L_\odot = 5.265$ and $P_4 = 181$ days at the shortest limit of the observed range 185 ± 4 days. The carbon abundance in the core of model D is 0.171, which will be exhausted in 260 years. At every stage of evolution from model D to B (carbon exhaustion), periods of excited pulsation modes agree with those of Betelgeuse. Model C is chosen as a typical model between B and D.

For the models of $v_i = 0.4v_{\text{crit}}$ we have listed only Model A in Table 2 although the $P_4 = 178$ days is slightly shorter than the observational limit (i.e., a slightly larger luminosity is needed to perfectly agree with P_4). The central carbon in model A is almost exhausted, and the luminosity and radius do not change any more to the carbon exhaustion phase.

We note that in the lower luminosity range $\log L/L_\odot < 2.52$, an additional shorter period mode (fourth overtone) is excited (right panel of Fig. 1), but it is not observed, which additionally supports a high luminosity of Betelgeuse.

The spatial amplitude variation of each excited mode in model C as an example is shown in Figure 2 (top and middle panels) by solid lines as a function of temperature in the envelope. In calculating linear pulsation modes we solve a set of equations with an eigenvalue σ , expressing the temporal variation of radial displacement as $\delta r \exp(i\sigma t)$, in which σ and δr (sometimes called the eigenfunction) are a complex number and a complex spatial function, respectively. The actual pulsation is expressed as the real part $[\delta r \exp(i\sigma t)]_r$ so that the imaginary part of δr expresses the deviation from the standing wave character in the envelope (i.e., zero points of displacement shift during a cycle of pulsation), and σ_1 (imaginary part of σ) gives the damping/growth rate of the pulsation mode. In contrast to the nearly adiabatic pulsations of the classical Cepheids, pulsations of supergiants are very non-adiabatic so that the imaginary parts of δr and σ can be comparable to the real parts.

The top panel of Figure 2 shows that δr of the longest period P_1 (2181 d) mode is nearly flat in the outermost layers decreasing

gently toward the center, which is exactly the property of radial fundamental mode. For this reason we identify P_1 as the fundamental mode (rather than LSP). The displacement of P_2 (434 d) mode has a dip at $\log T \approx 4.4$ corresponding to a node in the adiabatic pulsation, which indicates P_2 to be the first overtone mode. No clear nodes appear in strongly nonadiabatic pulsations, because zero points of real and imaginary parts of δr are separated. In the middle panel, δr (solid lines) P_3 and P_4 change rapidly with a few dips. We identify P_3 and P_4 as second and third overtones, respectively. We note that all pulsations are confined in the envelope of $\log T < 6$.

Note that $|\delta r|$'s for short period modes (for P_3 and P_4) in the middle panel of Figure 2 steeply change near the surface. This indicates that the pulsation energy of these modes leaks at the surface, for which we apply running-wave outer boundary condition in solving the eigenvalue problem. In spite of the leakage of energy, we find that these pulsations still grow (i.e., $\sigma_1 < 0$) because the driving in the inner part exceeds the energy loss at the surface.

4.2 Work integrals

A dashed line in the top or middle panel of Figure 2 presents the cumulative work W of each mode. The sign of the gradient dW/dr indicates whether the layer locally drives ($dW/dr > 0$) or damps ($dW/dr < 0$) the pulsation. Furthermore, whether W at the surface is positive or negative means the pulsation to be excited or damped in the model, respectively. The cumulative work $W(r)$ is calculated as (e.g., Saio & Cox 1980)

$$W(r) \propto \int_0^r r^2 P \text{Im} \left(\frac{\delta \rho}{\rho} \frac{\delta P^*}{P} \right) dr, \quad (1)$$

where P and ρ are pressure and density, respectively, while δ means the pulsational perturbation of the next quantity, and $\text{Im}(\dots)$ and $(^*)$ mean the imaginary part and the complex conjugate, respectively.

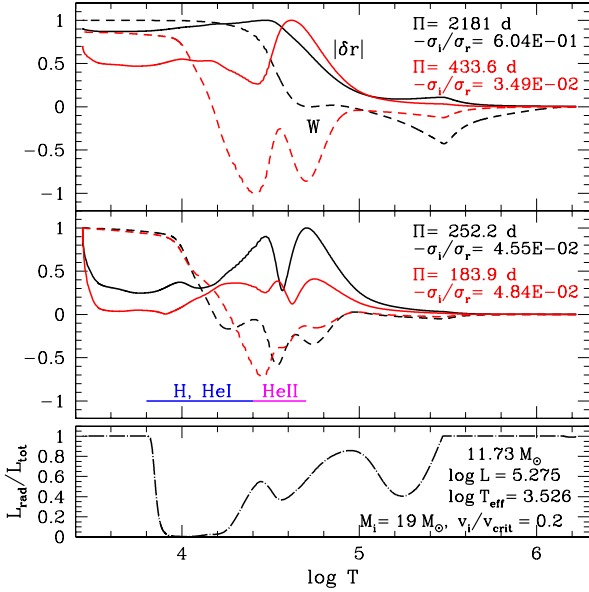


Figure 2. Pulsation properties of excited modes (upper panels) and radiative luminosity (bottom panel) versus logarithmic (base 10) temperature for model C (Table 2). The top and middle panels show the absolute value of radial displacements $|\delta r|$ normalized to their maximum value (solid lines) and (cumulative) work curves W (dashed lines). The ratio of imaginary to real parts of eigenfrequency σ_i/σ_r gives growth (if $\sigma_i < 0$) or damping ($\sigma_i > 0$) rates. The horizontal line in the middle panel indicates H,HeI (blue) and HeII (magenta) ionization zones. Red color is used to distinguish different modes plotted in one panel. The bottom panel shows the variation of the radiative to total luminosity ratio L_{rad}/L in the envelope.

Figure 2 indicates that the fundamental mode P_1 of Betelgeuse is mainly driven in the HeII ionization zone at $\log T \sim 4.5 - 4.6$, while for other shorter period modes the driving in the H/HeI ionization zone ($4.0 \leq \log T \leq 4.4$) is most important.

The bottom panel of Figure 2 shows the ratio of radiative to total luminosity, $L_{\text{rad}}/L_{\text{tot}}$, which is considerably smaller than unity in large ranges of the envelope indicating a significant fraction of the total energy flux to be carried by convection. The radiative/convective flux ratio affects the period as well as the driving/damping of the pulsation of a star with high luminosity to mass ratio, $L/M > 10^4$ (in solar units). Because the thermal time is comparable or shorter than the dynamical time in the envelope of such a luminous star, the pulsational variation of energy flux plays an important role to determine the pulsation period not only to excite or damp the pulsation. In fact, if we obtain pulsation periods of model C (Table 2) neglecting convective flux perturbations (which is sometimes called frozen convection approximation) we obtain periods of 1771, 409, 253, and 192 days. Comparing these periods with periods from the full calculations in model C, 2181, 434, 252, and 184 days, we find including convection flux perturbation to be important only for longer period pulsations in such luminous stars. This indicates that if we fitted the observed 2200-d period with the fundamental period obtained without convection effects, we would have a $\sim 17\%$ larger radius, because the pulsation period is approximately proportional to $R^{1.5}$. In addition, the fact that the convection effect is serious only in the fundamental mode suggests that even with a pulsation code without

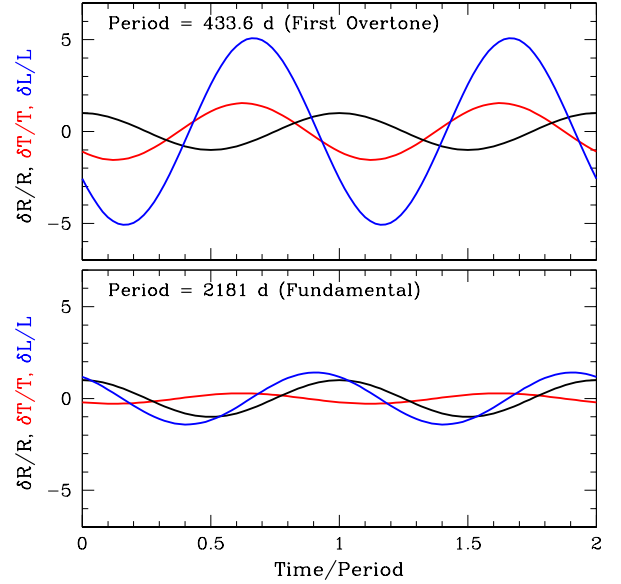


Figure 3. Periodic variations for $\delta R/R$ (black), $\delta T/T$ (red) and $\delta L/L$ (blue) at the surface, predicted by the linear perturbation analysis for the two lowest radial modes excited in model C (Table 2), while growth of amplitude is not included. The lower and the upper panels are for the fundamental (P_1) and first overtone (P_2) modes with periods of 2181 d and 433.6 d, respectively. The amplitudes are arbitrarily normalized as $\delta R/R = 1$ at $t = 0$ for both cases.

convection effects, we would have comparable asteroseismic models by using only overtone modes (i.e., avoiding the fundamental mode).

Figure 3 shows theoretical periodic variations of fractional radius (black), temperature (red), and luminosity (blue) at the surface for the radial fundamental mode P_1 (2181 d; lower panel) and the first overtone P_2 (433.6 d; upper panel) excited in model C (Table 2). The amplitudes are normalized as $\delta R/R = 1$ at $t = 0$ for both cases and fixed by suppressing a possible amplitude growth with time.

The amplitudes of the luminosity and the temperature variations of the P_1 mode are much smaller than the corresponding amplitudes of the P_2 mode. In addition, the luminosity maximum of P_1 mode occurs around the phase of maximum displacement $\delta R/R$, while for P_2 mode it occurs around minimum $\delta R/R$ when $\delta T/T$ is nearly maximum. The difference comes from the different strength of the non-adiabatic effects, which are stronger in the long-period P_1 mode than in the P_2 mode. Strong non-adiabaticity reduces the temperature variation significantly so that the radius effect in the luminosity variation

$$\delta L/L = 4\delta T_{\text{eff}}/T_{\text{eff}} + 2\delta R/R \quad (2)$$

exceeds the temperature effect. This explains why the luminosity maximum of the P_1 mode occurs around the maximum displacement $\delta R/R$. In contrast, for the shorter-period P_2 mode, the temperature perturbation to be large enough to exceed the effect of $\delta R/R$ effect so that the luminosity maximum occurs near the phase of temperature maximum.

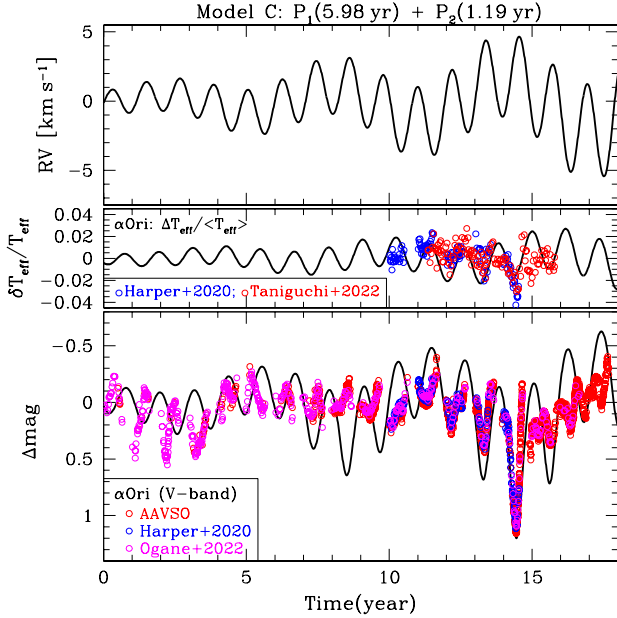


Figure 4. Radial velocity (RV;top), T_{eff} variation (middle) and brightness variation (bottom) versus time. The solid line in each panel is obtained by combining the fundamental (P_1) and the first-overtone (P_2) radial pulsations excited in model C (Table 2). The radial velocity in the top panel is set to be positive for 'red-shift'. The brightness variations in the bottom panel is normalized such that the maximum magnitude variation in this time range to be 1.2 mag, which also scales the amplitudes of model curves for RV and T_{eff} variations. The V-band magnitudes of Betelgeuse from AAVSO, Harper et al. (2020) and Ogane et al. (2022) are over-plotted, where the mean magnitude is assumed to be 0.5 mag and the observed dates are shifted by -2005.6 yr to fit with the model time. In the middle panel, relative deviations of T_{eff} from the mean $\langle T_{\text{eff}} \rangle$ of Betelgeuse obtained by Harper et al. (2020) and Taniguchi et al. (2022) are also plotted.

4.3 Synthesis of semi-periodic variation

All recent period analyses by various authors for the Betelgeuse light curves yielded at least periods P_1 and P_2 (see e.g. Table 1). This implies that the main features of the light variations of Betelgeuse should be qualitatively represented by a superposition of the periodic variations of P_1 and P_2 . In order to confirm the property, we have constructed a synthetic semi-periodic variation by adding the two pulsation modes (Figure 4). We have assumed arbitrarily that the two modes start (at $t = 0$) with the same amplitudes to each other. While a linear pulsation analysis assumes the (infinitesimal) amplitude proportional to $\exp(-\sigma_i t)$ with the imaginary part of the eigenfrequency $\sigma_i (< 0$ for an excited mode), we assume a slower growth as $(1 - \sigma_i t)$ because a rapid growth should be suppressed by non-linear effects for the (observable) finite amplitude pulsation. The radial velocity, RV is calculated as $-(2/3)\delta R/dt$, where a factor of $2/3$ presents the projection effect from the spherical surface. The RV variation (top panel) is plotted as red-shift (contraction) upward, and the luminosity variation is plotted in magnitude, $\Delta\text{mag} \equiv -2.5 \log(1 + \delta L/L)$, where $\delta R/R$ and $\delta L/L$ are sums of the two pulsation modes.

The 1.2-yr (P_2 ; first overtone) mode variations are modulated by the superposition of the 6.0-yr (P_1 ; fundamental) mode pulsation. The modulation amplitude grows with time as pulsation amplitudes grow. It is particularly interesting that the brightness variation (bottom panel of Fig. 4) has a deep minimum at $t \approx 14.5$ mimicking

the Great Dimming of Betelgeuse. To fit the luminosity minimum with the Great Dimming² we have normalized the luminosity variation such that $\Delta\text{mag} = 1.2$ mag at the minimum ($t = 14.5$) by multiplying a factor of $\delta L(t)$. RV(t) and $\delta T_{\text{eff}}(t)$ are scaled to be consistent with the luminosity variation. On the synthesized light curve, we have superposed V-band photometry results of Betelgeuse from various sources (indicated in this figure), in which all observed magnitudes are shifted by -0.5 mag (assuming the mean magnitude to be 0.5 mag), and observed time is shifted by -2005.6 yr to fit the time of the theoretical minimum (at 14.5 yr) with the Great Dimming at 2020.1 yr.

During the two cycles of P_2 prior to the Great Dimming, the synthesized light curve agrees with observation showing minima getting deeper, which seems to indicate the Great Dimming to be caused partially by a constructive interference between the fundamental and the first overtone pulsations (Guinan et al. 2019; Harper et al. 2020). Long before the Great Dimming the low-amplitude modulations associated with the fundamental mode (P_1) approximately trace the envelope of local maxima of the light variation. However, the phases of observational P_2 pulsation deviate considerably from the synthetic curve. This might mean that a phase modulation occurred in the first overtone (P_2) pulsation, or shorter period variations of P_3 and P_4 , not included in our synthetic light curve, significantly modify the first overtone pulsation.

Just after the Great Dimming, the P_2 (434-d) pulsation suddenly became invisible and is replaced with low-amplitude shorter timescale ~ 200 -d variations (Dupree et al. 2022; Jadrlovský et al. 2023), while the fundamental mode (P_1) pulsation seems to remain intact. This disappearance of the first-overtone pulsation may suggest that a massive mass loss (Jadrlovský et al. 2023; Dupree et al. 2022) at the Great Dimming disturbed significantly the P_2 pulsation. Since the growth time of the first-overtone pulsation is about 5.4 yr (Fig. 2), the 434-d pulsation may appear again around 2025. MacLeod et al. (2023) also predicts the re-appearance of the ~ 400 -d pulsation in a similar timescale (5–10 years) although they regard it as fundamental mode.

The predicted effective temperature variation (middle panel of Figure 4) hardly modulates with the period P_1 . This is understood as that the temperature variation of the fundamental mode (corresponding to P_1) is suppressed significantly due to the strong nonadiabatic effect as seen in Figure 3. Effective temperature variations of Betelgeuse obtained by Harper et al. (2020) and Taniguchi et al. (2022) are plotted for comparison. While observed results have some wiggles that are probably caused by shorter period pulsations not considered here, the observed range of T_{eff} variations are comparable with our simple two-mode prediction. We note that Wasatonic (2022) and Mittag et al. (2023) also obtained similar variations in the effective temperature of Betelgeuse.

Around the Great Dimming, the synthesized RV curve (top panel) attains maximum (red-shift) 0.1-yr after the minimum brightness. This phase relation agrees with the observed relation (Dupree et al. 2022; MacLeod et al. 2023). Our two-mode synthesis predicts 4.5 km s^{-1} at the maximum, which is comparable with observed values (Kravchenko et al. 2021; Dupree et al. 2022). However, the observed minimum RV (maximum expansion velocity) about -6 km s^{-1} that occurred ~ 200 -d before the Great Dimming is smaller

² Although complicated phenomena such as dark spots and dust formation occurred during the Great Dimming as summarized in Wheeler & Chatzopoulos (2023), here for simplicity, we have taken into account only pulsational variations for our qualitative synthetic light curve.

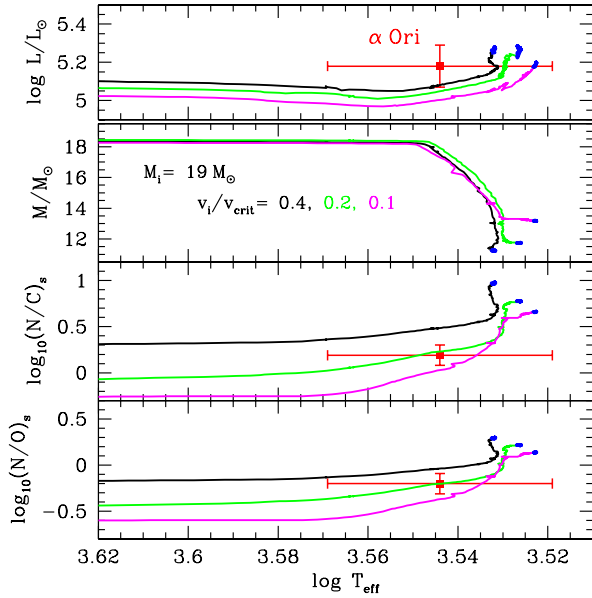


Figure 5. Evolutions of luminosity, mass, and surface CNO ratios for an initial mass of $19 M_{\odot}$ are compared with the observational data of Betelgeuse (α Ori). Various cases of the initial rotation frequency versus critical one v_i/v_{crit} are color coded as shown in the second panel from the top. The core carbon burning stage is indicated by blue color. The abundance ratios N/C and N/O stand for the number ratios, while observed ones are adopted from Carr et al. (2000).

than our model prediction -1 km s^{-1} . The discrepancy may be consistent with the emergence of a shock in the expansion phase found by Kravchenko et al. (2021) and Dupree et al. (2022), or a breakout of a convective plume as discussed in MacLeod et al. (2023). While various complex phenomena are involved in the RV variations, the diameter of Betelgeuse seems to change by $5 \sim 10\%$ on time-scales comparable to pulsation periods (Townes et al. 2009; Taniguchi et al. 2022).

4.4 Surface CNO abundance

Figure 5 shows the evolutions of luminosity, mass, and CNO abundance ratios at the surface for models with different initial (at ZAMS) rotation velocity given as $v_i/v_{\text{crit}} = 0.4, 0.2, 0.1$ ($M_i = 19 M_{\odot}$). The second panel from the top shows that the mass-loss occurs mainly in the red-supergiant range (core He burning stage), where up to $6 M_{\odot}$ is lost. The lost mass is larger for a larger v_i because of a larger luminosity associated with larger helium core, which was produced by extensive rotational mixing around the convective core during the main-sequence evolution.

Because of the large mass loss in the red-supergiant stage, CNO processed matter emerges to the surface and increases N/C and N/O ratios. The N/C and N/O ratios of the models in the core carbon burning stage, whose pulsation periods agree well with the observed periods of Betelgeuse, are, unfortunately, larger than the observed values obtained by Carr et al. (2000). As a numerical example, the model predicts a N/C that is 0.5 dex larger than measured. This discrepancy seems to indicate that the rotational diffusive mixing is overestimated. The present computation has been performed using specific choices for the diffusion coefficients describing the trans-

port by shear turbulence and meridional currents (see references in Ekström et al. 2012). The choice made in the present computation actually favors the mixing. Other choices would have produced smaller results. As a numerical example, models of $15 M_{\odot}$ with an initial rotation equal to 40% the critical velocity at solar metallicity have been computed with different choices of these diffusion coefficients (see Nandal et al. 2023 in preparation). The N/C ratio at the surface when $\log T_{\text{eff}} = 3.6$ can be reduced up to 0.5 dex changing the expressions of the diffusion coefficients describing the shear mixing. Thus indeed, the solution to that problem can be linked to the specific physics used here for rotational mixing. These models would however present similar structure of their envelope at the red supergiant stage and thus we do not expect this will influence the properties of the pulsation modes during that stage.

5 DISCUSSION

Our models that excite four radial pulsations consistent with observed four periods of Betelgeuse (Table 2) have radii larger than $1200 R_{\odot}$, which are much larger than the previous estimates based on seismological predictions (~ 700 to $\sim 900 R_{\odot}$) by Joyce et al. (2020) and Dolan et al. (2016). The difference arises from the fact that the previous analysis fitted the period P_2 (~ 420 d) with the period of the radial fundamental pulsation, regarding the periodicity P_1 (~ 2200 d) to be a non-pulsational origin. In contrast, we have fitted the period P_1 with the fundamental non-adiabatic pulsation period of a core-carbon-burning model having a radius of $\sim 1300 R_{\odot}$ (Table 2). The model excites not only the fundamental mode which fits with P_1 but also excites the first, second, and third overtones whose periods agree with the observed periods P_2 , P_3 , and P_4 , respectively.

The large radii of our models have some supports from some of the interferometric observations of the angular diameter, although the determinations are affected by various complex factors (Dolan et al. 2016). Haubois et al. (2009) obtained the Rosseland angular diameter of Betelgeuse to be 45.03 ± 0.12 mas which was confirmed by Neilson et al. (2011). Combining the angular diameter with the distance 222_{-34}^{+48} pc (Harper et al. 2017) yields $R(\alpha \text{ Ori}) = 1074_{-165}^{+232} R_{\odot}$, which is consistent with our models in Table 2. Furthermore, Cannon et al. (2023) obtained an angular diameter of 59.02 ± 0.64 mas in the spectral range between 8 and $8.75 \mu\text{m}$, which corresponds to a radius $1409_{-229}^{+319} R_{\odot}$ at the same distance as above, while it is known that measurements with longer wavelength yield larger angular diameters. ³

Furthermore, fitting interferometric observations with the limb-darkening law, Neilson et al. (2011) obtained the radius to mass ratio $R/M = 82.17_{-11.51}^{+13.32} R_{\odot}/M_{\odot}$, while our models in Table 2 give $R/M = 110 \pm 2 R_{\odot}/M_{\odot}$. Although R/M of our models are slightly larger than the Neilson et al. (2011)’s estimate, we do not think the difference serious because the mass-loss rate assumed as a function of stellar parameters certainly has some deviations from the real mass-loss rates. Lobel & Dupree (2000) obtained a surface gravity of $\log g = -0.5$ from metal absorption lines of Betelgeuse, while our models in Table 2 have $\log g = -0.7$. We consider that the difference is not serious, because a typical uncertainty in the measurements of $\log g$ is ± 0.2 (e.g. Smalley 2005).

Kervella et al. (2018) estimated an equatorial rotation velocity of

³ Molnár et al. (2023) claims that the radius of Betelgeuse should be limited to $< 1100 R_{\odot}$. However, we do not consider the limit to be seriously discrepant to the Haubois et al. (2009)’s result, because various uncertainties would enter in the measurements of the angular diameter.

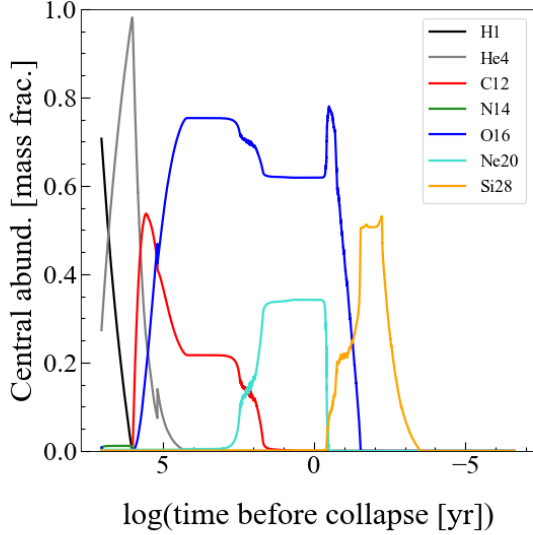


Figure 6. Central abundances of various elements versus time (in logarithm of base 10) to collapse for the model of $M_i = 19 M_\odot$ with the initial rotation velocity $v_i = 0.2 v_{\text{crit}}$.

$v_{\text{eq}} = 6.5_{-0.8}^{+4.1} \text{ km s}^{-1}$. In contrast, our models of Betelgeuse have rotation velocity less than 0.1 km s^{-1} even if they were rotating at 40% of critical value at the ZAMS stage. The lack of rotation is common to the single-star models of Betelgeuse, as [Wheeler et al. \(2017\)](#) proposes a merger with another star to get additional angular momentum (see also [Sullivan et al. 2020](#)).

Recently, [Neuhäuser et al. \(2022\)](#) claimed to find evidences in pre-telescopic records suggesting that the color of Betelgeuse was yellow 2000 yr ago. Based on the evolution models by [Choi et al. \(2016\)](#), they concluded that Betelgeuse having an initial mass of $\sim 14 M_\odot$ crossed the Hertzsprung gap 1000 years ago and settled in the early stage of He burning. Their interpretation contradicts with our carbon-burning models. However, we do not consider their interpretation unique. We discuss here another possibility associated with a blue loop from the red supergiant branch. The surface-temperature evolution of supergiants is very sensitive to the interior-chemical composition gradients, envelope mass (or mass-loss rates), core mass, etc. A small or large blue loop can occur depending on subtle differences in these parameters as shown in [Georgy \(2012\)](#) and [Meynet et al. \(2013, 2015\)](#). These evolutions are not well understood theoretically. Observationally, it is known that the progenitors of some Type II supernovae were yellow supergiants ([Georgy 2012](#); [Smartt 2015](#)), which indicates blue loops to actually occur even in the very late evolutionary stage. Therefore, we interpret [Neuhäuser et al. \(2022\)](#)'s finding as that Betelgeuse returned recently from such a blue-loop evolution. Although our models do not have blue loops, we may be able to have a blue loop during the red-supergiant evolution by tuning parameters, which we leave for the future research.

We have found that four periods of the photometric variations of Betelgeuse are consistent with the four lowest order radial pulsations in the carbon burning models which evolved from an initial stellar mass of $19 M_\odot$. As shown in [Table 2](#), the evolution stage can be very close to the carbon exhaustion (as models A, B, and C). In

fact, it is not possible to determine the exact evolutionary stage, because surface conditions hardly change in the late stage close to the carbon exhaustion and beyond, while the property of radial pulsation depends only in the envelope structure. To see the time to a core-collapse after the core carbon exhaustion, we have extended the evolution for the model with $v_i = 0.2 v_{\text{crit}}$ to the silicon exhaustion. [Figure 6](#) depicts the central abundance of elements of the model versus time to the collapse. In model D, the central carbon would be exhausted in about 260 years, while less time is needed in the other models in [Table 2](#). After the central carbon exhaustion, [Figure 6](#) indicates that the core will collapse in a few tens of years. This suggests Betelgeuse to be a good candidate for the next Galactic supernova which occurs very near to us.

Recently, the supernova SN2023ixf is discovered in the nearby galaxy M101 ([Itagaki 2023](#)). Interestingly, the pre-explosion observation archives show that the progenitor of the supernova was a pulsating red supergiant, for which [Jencson et al. \(2023\)](#) obtained the period $1119.4_{-233.3}^{+132.4}$ days and the luminosity $\log L/L_\odot = 5.1 \pm 0.2$ (similar period and luminosity were also obtained by [Soraisam et al. 2023](#)). For comparison, the period range is shown in [Figure 1](#) by a horizontal gray line. The position in the PL relation suggests that the progenitor of SN2023ixf might be slightly less massive compared with Betelgeuse, which is consistent with the initial mass $17 \pm 4 M_\odot$ estimated by [Jencson et al. \(2023\)](#).

6 CONCLUSION

We have found carbon-burning models that excite the radial fundamental mode, as well as the first, second, and third overtones. The periods excited pulsation modes agree with periods of 2190, 417, 230, and 185 d that had been detected in Betelgeuse. On the HR diagram, these models are located within the allowed range of effective temperature and luminosity of Betelgeuse. Beginning with a mass of $19 M_\odot$ at ZAMS (with a rotation velocity of 0.2 or $0.4 v_{\text{crit}}$), the models lose significant mass mainly in the core-He burning stage to have a mass of $11 \sim 12 M_\odot$ in the core carbon-burning stage. A large radius of about $1300 R_\odot$ (needed for the long-period fundamental mode) is supported by some interferometric measurements of the angular diameter combined with the distance 222_{-34}^{+48} pc ([Harper et al. 2017](#)). We conclude that according to our seismic and evolutionary models Betelgeuse is likely in a late phase (or near the end) of the core carbon burning. After carbon is exhausted (likely in less than ~ 300 years) in the core, a core-collapse leading to a supernova explosion is expected in a few tens of years.

ACKNOWLEDGEMENTS

The authors thank Dr Nami Mowlavi for interesting discussions on the identification of the pulsation modes of Betelgeuse. We also thank Daisuke Taniguchi for allowing us to use the T_{eff} data presented in [Taniguchi et al. \(2022\)](#). We acknowledge with thanks the variable star observations from the AAVSO International Database contributed by observers worldwide and used in this research. DN, GM, and SE have received funding from the European Research Council (ERC) under the European Union's Horizon 2020 research and innovation program (grant agreement No 833925, project STAREX).

DATA AVAILABILITY

The data underlying this article and pulsation code will be shared on reasonable request to the authors, while some interactive instructions how to use it would be needed for the latter.

REFERENCES

- Anderson R. I., Saio H., Ekström S., Georgy C., Meynet G., 2016, *A&A*, **591**, A8
- Cannon E., et al., 2023, *arXiv e-prints*, p. arXiv:2303.08892
- Carr J. S., Sellgren K., Balachandran S. C., 2000, *ApJ*, **530**, 307
- Chatys F. W., Bedding T. R., Murphy S. J., Kiss L. L., Dobie D., Grindlay J. E., 2019, *MNRAS*, **487**, 4832
- Choi J., Dotter A., Conroy C., Cantiello M., Paxton B., Johnson B. D., 2016, *ApJ*, **823**, 102
- Cutri R. M., et al., 2003, VizieR Online Data Catalog, p. II/246
- Dharmawardena T. E., Mairs S., Scicluna P., Bell G., McDonald I., Menten K., Weiss A., Zijlstra A., 2020, *ApJ*, **897**, L9
- Dolan M. M., Mathews G. J., Lam D. D., Quynh Lan N., Herczeg G. J., Dearborn D. S. P., 2016, *ApJ*, **819**, 7
- Dupree A. K., et al., 2022, *ApJ*, **936**, 18
- Ekström S., et al., 2012, *A&A*, **537**, A146
- Gabriel M., Scuflaire R., Noels A., Boury A., 1975, *A&A*, **40**, 33
- Georgy C., 2012, *A&A*, **538**, L8
- Gonczy G., Osaki Y., 1980, *A&A*, **84**, 304
- Granger T., Weber M., Strassmeier K. G., Dupree A., 2022, in Cambridge Workshop on Cool Stars, Stellar Systems, and the Sun. Cambridge Workshop on Cool Stars, Stellar Systems, and the Sun. p. 185, doi:10.5281/zenodo.7589936
- Grigahcène A., Dupret M. A., Gabriel M., Garrido R., Scuflaire R., 2005, *A&A*, **434**, 1055
- Guinan E. F., Wasatonic R. J., Calderwood T. J., 2019, The Astronomer's Telegram, **13365**, 1
- Harper G. M., Brown A., Guinan E. F., O'Gorman E., Richards A. M. S., Kervella P., Decin L., 2017, *AJ*, **154**, 11
- Harper G. M., Guinan E. F., Wasatonic R., Ryde N., 2020, *ApJ*, **905**, 34
- Haubois X., et al., 2009, *A&A*, **508**, 923
- Henyey L., Vardya M. S., Bodenheimer P., 1965, *ApJ*, **142**, 841
- Itagaki K., 2023, Transient Name Server Discovery Report, 2023-1158, 1
- Jadlovský D., Krtička J., Paurzen E., Štefl V., 2023, *New Astron.*, **99**, 101962
- Jencson J. E., et al., 2023, *arXiv e-prints*, p. arXiv:2306.08678
- Josselin E., Blommaert J. A. D. L., Groenewegen M. A. T., Omont A., Li F. L., 2000, *A&A*, **357**, 225
- Joyce M., Leung S.-C., Molnár L., Ireland M., Kobayashi C., Nomoto K., 2020, *ApJ*, **902**, 63
- Kervella P., et al., 2018, *A&A*, **609**, A67
- Kiss L. L., Szabó G. M., Bedding T. R., 2006, *MNRAS*, **372**, 1721
- Kravchenko K., et al., 2021, *A&A*, **650**, L17
- Levesque E. M., Massey P., 2020, *ApJ*, **891**, L37
- Levesque E. M., Massey P., Olsen K. A. G., Plez B., Josselin E., Maeder A., Meynet G., 2005, *ApJ*, **628**, 973
- Lobel A., Dupree A. K., 2000, *ApJ*, **545**, 454
- Luo T., Umeda H., Yoshida T., Takahashi K., 2022, *ApJ*, **927**, 115
- MacLeod M., Antoni A., Huang C. D., Dupree A., Loeb A., 2023, *arXiv e-prints*, p. arXiv:2305.09732
- Meynet G., Haemmerlé L., Ekström S., Georgy C., Groh J., Maeder A., 2013, in Kervella P., Le Bertre T., Perrin G., eds, EAS Publications Series Vol. 60, EAS Publications Series. pp 17–28 (arXiv:1303.1339), doi:10.1051/eas/1360002
- Meynet G., et al., 2015, *A&A*, **575**, A60
- Mittag M., Schröder K. P., Perdelwitz V., Jack D., Schmitt J. H. M. M., 2023, *A&A*, **669**, A9
- Molnár L., Joyce M., Leung S.-C., 2023, *Research Notes of the American Astronomical Society*, **7**, 119
- Montargès M., et al., 2021, *Nature*, **594**, 365
- Nance S., Sullivan J. M., Diaz M., Wheeler J. C., 2018, *MNRAS*, **479**, 251

- Neilson H. R., Lester J. B., Haubois X., 2011, in Qain S., Leung K., Zhu L., Kwok S., eds, Astronomical Society of the Pacific Conference Series Vol. 451, 9th Pacific Rim Conference on Stellar Astrophysics. p. 117 (arXiv:1109.4562), doi:10.48550/arXiv.1109.4562
- Neuhäuser R., Torres G., Mugrauer M., Neuhäuser D. L., Chapman J., Luge D., Cosci M., 2022, *MNRAS*, **516**, 693
- Ogane Y., Ohshima O., Taniguchi D., Takanashi N., 2022, *Open European Journal on Variable Stars*, **233**, 1
- Saio H., 1980, *ApJ*, **240**, 685
- Saio H., Cox J. P., 1980, *ApJ*, **236**, 549
- Saio H., Winget D. E., Robinson E. L., 1983, *ApJ*, **265**, 982
- Smalley B., 2005, *Memorie della Societa Astronomica Italiana Supplementi*, **8**, 130
- Smartt S. J., 2015, *Publ. Astron. Soc. Australia*, **32**, e016
- Soraisam M. D., et al., 2023, *arXiv e-prints*, p. arXiv:2306.10783
- Stothers R., Leung K. C., 1971, *A&A*, **10**, 290
- Sullivan J. M., Nance S., Wheeler J. C., 2020, *ApJ*, **905**, 128
- Taniguchi D., Yamazaki K., Uno S., 2022, *Nature Astronomy*, **6**, 930
- Townes C. H., Wishnow E. H., Hale D. D. S., Walp B., 2009, *ApJ*, **697**, L127
- Trabucchi M., Wood P. R., Montalbán J., Marigo P., Pastorelli G., Girardi L., 2017, *ApJ*, **847**, 139
- Unno W., 1967, *PASJ*, **19**, 140
- Wasatonic R., 2022, *JAAVSO*, **50**, 205
- Wheeler J. C., Chatzopoulos E., 2023, *arXiv e-prints*, p. arXiv:2306.09449
- Wheeler J. C., et al., 2017, *MNRAS*, **465**, 2654
- Yusof N., et al., 2022, *MNRAS*, **511**, 2814

APPENDIX A: RADIAL PULSATION COUPLED WITH CONVECTION

In this appendix we derive differential equations to solve radial pulsations taking into account the coupling with convection based on the mixing-length theory. In the beginning we follow Unno (1967)'s discussion but later we include additional terms to avoid rapid oscillations where the turnover time is longer than the pulsation period (e.g. Grigahcène et al. 2005). We summarise differential equations of radial pulsations in the last part of this appendix.

A1 Basic Equations

Equations of motion and mass conservation, including convective motion can be written as

$$(\rho + \rho') \left[\frac{\partial}{\partial t} + (\mathbf{u} + \mathbf{V}_c) \cdot \nabla \right] (\mathbf{u} + \mathbf{V}_c) = -\nabla(P + P') - (\rho + \rho') \nabla \psi \quad (\text{A1})$$

and

$$\frac{\partial(\rho + \rho')}{\partial t} + \nabla \cdot [(\rho + \rho')(\mathbf{u} + \mathbf{V}_c)] = 0, \quad (\text{A2})$$

where \mathbf{u} and \mathbf{V}_c are pulsation and convection velocities, respectively, and a prime ' such as ρ' , P' , T' , etc means the convective Eulerian perturbation. We neglect convective perturbation of the gravitational potential ψ .

Conservation of thermal energy can be written as

$$(\rho + \rho')(T + T') \left[\frac{\partial}{\partial t} + (\mathbf{u} + \mathbf{V}_c) \cdot \nabla \right] (S + S') = \rho \epsilon_n + (\rho \epsilon_n)' - \nabla \cdot (\mathbf{F}_{\text{rad}} + \mathbf{F}'_{\text{rad}}), \quad (\text{A3})$$

where S and ϵ_n are the entropy and the nuclear energy generation rate per unit mass, respectively, and \mathbf{F}_{rad} is the radiative energy flux.

A2 Equations for mean fluid

Taking a horizontal average ($\overline{V_c} = 0, \overline{(\dots)'} = 0$) of equation(A1), and assuming the Boussinesq approximation for convection motions, we have

$$\rho \frac{d\mathbf{u}}{dt} + \rho \overline{V_c \cdot \nabla V_c} = -\nabla P - \rho \nabla \psi, \quad (\text{A4})$$

where the second term on the left-hand-side is the turbulent stress, where we have defined

$$\frac{d}{dt} = \frac{\partial}{\partial t} + \mathbf{u} \cdot \nabla. \quad (\text{A5})$$

Similarly, taking horizontal averages of equations (A2) and (A3) we obtain

$$\frac{d\rho}{dt} + \rho \nabla \cdot \mathbf{u} = 0. \quad (\text{A6})$$

and

$$\rho T \frac{dS}{dt} + \rho T \overline{V_c \cdot \nabla S'} = \rho \epsilon_n - \nabla \cdot \mathbf{F}_{\text{rad}}, \quad (\text{A7})$$

where we have assumed that $|T'| \ll T$ and $|\rho'| \ll \rho$. Since $\nabla \cdot V_c = 0$ (Boussinesq approximation) and hence $V_c \cdot \nabla S' = \nabla \cdot (V_c S')$, we approximately write equation (A7) as

$$\rho T \frac{dS}{dt} = \rho \epsilon_n - \nabla \cdot \mathbf{F}_{\text{rad}} - \nabla \cdot \mathbf{F}_{\text{con}}, \quad (\text{A8})$$

with defining the convective flux as

$$\mathbf{F}_{\text{con}} \equiv \rho T \overline{V_c S'} = \rho C_p \overline{V_c T'} \quad (\text{A9})$$

(Unno 1967). Considering the pulsational Lagrangian perturbations δ and keeping only linear terms we have

$$\delta \mathbf{F}_{\text{con}} = \mathbf{F}_{\text{con}0} \left(\frac{\delta \rho}{\rho} + \frac{\delta T}{T} \right) + \rho T [(\overline{\delta V_c}) S' + \overline{V_c \delta S'}]. \quad (\text{A10})$$

In the equilibrium condition the mean convective flux has only radial direction,

$$\mathbf{F}_{\text{con}0} = \mathbf{e}_r \rho T \overline{V_c' S'}. \quad (\text{A11})$$

We can write equation (A10) as

$$\frac{\delta \mathbf{F}_{\text{con}}}{F_{\text{con}0}} = \left(\frac{\delta \rho}{\rho} + \frac{\delta T}{T} \right) \mathbf{e}_r + \frac{\delta V_c}{V_c'} + \frac{\overline{V_c \delta S'}}{V_c' S'} \quad (\text{A12})$$

For radial pulsations, $\mathbf{u} = u \mathbf{e}_r$, we have

$$\frac{\delta F_{\text{con}}}{F_{\text{con}}} = \left(\frac{\delta \rho}{\rho} + \frac{\delta T}{T} \right) + \frac{\delta V_c'}{V_c'} + \frac{\delta S'}{S'} \quad (\text{A13})$$

Then, we have

$$\delta(\nabla \cdot \mathbf{F}_{\text{con}}) = \frac{1}{r^2} \frac{d(r^2 \delta F_{\text{con}})}{dr} - \frac{d\xi_r}{dr} \frac{dF_{\text{con}}}{dr} - \frac{2\xi_r}{r^2} F_{\text{con}}, \quad (\text{A14})$$

where ξ_r stands for the radial displacement of pulsation.

A3 Equations for time-dependent convection

A3.1 Mechanical equations

Subtracting equation (A4) from equation (A1) and neglecting a non-linear term $\rho \mathbf{u} \cdot \nabla \mathbf{u}$, we obtain

$$\rho \frac{dV_c}{dt} + \rho (V_c \cdot \nabla V_c - \overline{V_c \cdot \nabla V_c}) + \rho V_c \cdot \nabla \mathbf{u} = -\nabla P' - \rho' \nabla \psi. \quad (\text{A15})$$

Here we have disregard ρ' in the left hand side of equation (A1), because we are using the Boussinesq approximation for convective motion. Following Unno (1967)'s conjecture that convection motion

would approach to equilibrium in a time scale of the turnover time of convective eddies, we assume that

$$V_c \cdot \nabla V_c - \overline{V_c \cdot \nabla V_c} = \alpha \left(\frac{1}{\tau} + \sigma_r \right) V_c, \quad (\text{A16})$$

where α is a numerical parameter of order one, and τ is the turnover time of convective eddies, which may be written as

$$\tau = \ell / v \quad (\text{A17})$$

with mixing length ℓ and $v \equiv \overline{|V_c'|}$.

We have included σ_r (the real part of pulsation frequency) in equation (A16) in addition to Unno (1967)'s original $1/\tau$ term, in order to prevent rapid spacial oscillations in pulsation amplitude that occur near the bottom of the convection zone (where $\tau \gg 1/\sigma_r$) (Gonczi & Osaki 1980; Grigahcène et al. 2005). This modification comes from the conjecture that if the pulsation period is much shorter than the turn-over time τ (associated with largest eddies), smaller scale eddies having time-scales of $\sim 1/\sigma_r$ would be important (Saio 1980). Similar assumption was adopted by Grigahcène et al. (2005). Substituting equation (A16) into equation (A15) we obtain

$$\frac{dV_c}{dt} = -\alpha \left(\frac{1}{\tau} + \sigma_r \right) V_c - V_c \cdot \nabla \mathbf{u} - \frac{1}{\rho} \nabla P' - \frac{\rho'}{\rho} \nabla \psi. \quad (\text{A18})$$

For mass conservation of convection motion, we adopt Boussinesq approximation

$$\nabla \cdot V_c = 0. \quad (\text{A19})$$

A3.2 Thermal equations

Subtracting equation(A7) from equation(A3) we obtain

$$\rho T \left[\frac{dS'}{dt} + V_c \cdot \nabla S \right] + (\rho T)' \frac{dS}{dt} + \rho T (V_c \cdot \nabla S' - \overline{V_c \cdot \nabla S'}) = (\rho \epsilon_n)' - \nabla \cdot \mathbf{F}'_{\text{rad}} \quad (\text{A20})$$

Similarly to equation (A16), we assume that

$$V_c \cdot \nabla S' - \overline{V_c \cdot \nabla S'} = \beta \left(\frac{1}{\tau} + \sigma_r \right) S', \quad (\text{A21})$$

where β is another numerical parameter of order one. Then we obtain

$$\frac{dS'}{dt} + V_c \cdot \nabla S + \left(\frac{T'}{T} + \frac{\rho'}{\rho} \right) \frac{dS}{dt} + \beta \left(\frac{1}{\tau} + \sigma_r \right) S' = -\frac{1}{\rho T} \nabla \cdot \mathbf{F}'_{\text{rad}} \quad (\text{A22})$$

where we neglected the term $(\rho \epsilon_n)'$ because we are interested only in the envelope convection. For the last term of the above equation we assume

$$\nabla \cdot \mathbf{F}'_{\text{rad}} \approx -\frac{4acT^3}{3\kappa\rho} \nabla^2 T' \approx \frac{4acT^3}{3\kappa\rho} \frac{T'}{(\ell^2/f)}, \quad (\text{A23})$$

where κ is opacity per unit mass, ℓ mixing length, and f is a numerical factor; its appropriate value will be discussed in the next subsection.

Furthermore, according to the assumptions in the mixing-length theory, we assume $P' \approx 0$ in obtaining convective perturbations of the thermodynamic relations (but P' is retained in the equation of motion discussed below). Then, we have

$$\frac{T'}{T} \approx \left(\frac{\partial \ln T}{\partial S} \right)_P S' = \frac{S'}{C_p}, \quad (\text{A24})$$

and

$$\nabla \cdot \mathbf{F}'_{\text{rad}} \approx \frac{4acT^4}{3\kappa\rho C_p} \frac{S'}{(\ell^2/f)} = \rho T K_{\text{rad}} S', \quad (\text{A25})$$

with

$$K_{\text{rad}} \equiv \frac{4acT^3}{3\kappa\rho^2 C_p (\ell^2/f)}. \quad (\text{A26})$$

Under the same assumption, we can write the density perturbation as

$$\frac{\rho'}{\rho} \approx \left(\frac{\partial \ln \rho}{\partial \ln T} \right)_P \frac{T'}{T} = -\frac{\chi_T}{\chi_\rho} \frac{T'}{T} = -\frac{\chi_T}{\chi_\rho} \frac{S'}{C_p}. \quad (\text{A27})$$

Then we obtain

$$\rho T' + T \rho' \approx \rho T \left(1 - \frac{\chi_T}{\chi_\rho} \right) \frac{S'}{C_p}, \quad (\text{A28})$$

where $\chi_T \equiv (\partial \ln P / \partial \ln T)_\rho$ and $\chi_\rho \equiv (\partial \ln P / \partial \ln \rho)_T$. Using these relations in eq. (A22), we obtain

$$\frac{dS'}{dt} + \mathbf{V}_c \cdot \nabla S + \left(1 - \frac{\chi_T}{\chi_\rho} \right) \frac{S'}{C_p} \frac{dS}{dt} + \left(\frac{\beta}{\tau} + \beta\sigma_r + K_{\text{rad}} \right) S' = 0. \quad (\text{A29})$$

A3.3 Convection in equilibrium

In this subsection we discuss the relation between our formulations and the mixing-length theory to obtain relations among the parameters α , β and convective eddy shapes. If there is no pulsation we have steady-state convection, in which \mathbf{V}_{c0} is given from equation (A18)

$$\frac{\alpha}{\tau} \mathbf{V}_{c0} = -\frac{1}{\rho} \nabla P'_0 - \frac{\rho'_0}{\rho} \nabla \psi. \quad (\text{A30})$$

Treating the convective motion locally by replacing ∇ with $i\mathbf{k}$, we obtain the radial component of convection velocity V_{c0}^r

$$\frac{\alpha}{\tau} V_{c0}^r = -ik_r \left(\frac{P'}{\rho} \right)_0 - g \left(\frac{\rho'}{\rho} \right)_0 \quad (\text{A31})$$

and the horizontal component \mathbf{V}_{c0}^h

$$\mathbf{V}_{c0}^h = -i \frac{\tau}{\alpha} \mathbf{k}_h \left(\frac{P'}{\rho} \right)_0. \quad (\text{A32})$$

The continuity equation $\nabla \cdot \mathbf{V}_{c0} = 0$ can be written as

$$k_r V_{c0}^r + \mathbf{k}_h \cdot \mathbf{V}_{c0}^h = 0. \quad (\text{A33})$$

Combining equations (A32) and (A33), we obtain

$$ik_r \left(\frac{P'}{\rho} \right)_0 = \frac{k_r^2}{k_h^2} \frac{\alpha V_{c0}^r}{\tau}. \quad (\text{A34})$$

Substituting this equation into the first relation in equation (A31), we obtain

$$\left(\frac{\rho'}{\rho} \right)_0 = -\frac{\alpha}{\tau g} \frac{k^2}{k_h^2} V_{c0}^r \quad \text{or} \quad \left(\frac{S'}{C_p} \right)_0 \frac{\chi_T}{\chi_\rho} = \frac{\alpha}{\tau g} \frac{k^2}{k_h^2} V_{c0}^r, \quad (\text{A35})$$

where $k^2 = k_r^2 + k_h^2$.

In the equilibrium state eq. (A29) can be written as

$$V_{c0}^r \frac{dS_0}{dr} = -\left(\frac{\beta}{\tau} + K_{\text{rad}} \right) S'_0. \quad (\text{A36})$$

Since

$$\frac{dS_0}{dr} = -\frac{C_p}{H_p} (\nabla - \nabla_{\text{ad}}), \quad (\text{A37})$$

equation (A36) may be written as

$$\left(\frac{\beta}{\tau} + K_{\text{rad}} \right) S'_0 = V_{c0}^r \frac{C_p}{H_p} (\nabla - \nabla_{\text{ad}}). \quad (\text{A38})$$

A relation with the mixing length theory is apparent if we have the horizontal average of the absolute value and use the relation $|\overline{V_{c0}^r}| = v = \ell/\tau$,

$$\frac{|\overline{S'_0}|}{C_p} = \frac{|\overline{T'_0}|}{T} = \frac{1}{\beta} \frac{1}{1 + (\tau K_{\text{rad}}/\beta)} (\nabla - \nabla_{\text{ad}}) \frac{\ell}{H_p}. \quad (\text{A39})$$

In the formulation of MLT by [Heney et al. \(1965\)](#) the efficiency factor γ defined as

$$\gamma = \frac{\nabla - \nabla'}{\nabla' - \nabla_{\text{ad}}} \rightarrow \nabla - \nabla' = \frac{\gamma}{\gamma + 1} (\nabla - \nabla_{\text{ad}}), \quad (\text{A40})$$

where ∇' is the temperature gradient felt by moving eddies (sometimes called internal temperature gradient).

According to eq.(36) in [Heney et al. \(1965\)](#)(their opacity per unit volume is converted to the opacity per unit mass here), for optically thick convective eddies,

$$\frac{1}{\gamma} = \frac{2acT^3}{C_p v \kappa \rho^2 \ell y} = \frac{3}{2} K_{\text{rad}} \frac{\tau}{y f} \quad (\text{A41})$$

with $y = 3/(4\pi^2)$. If we set $f = 2\pi^2\beta$, we have $\tau K_{\text{rad}}/\beta = 1/\gamma$. Then equation (A39) becomes

$$\frac{|\overline{T'_0}|}{T} = \frac{1}{\beta} \frac{\gamma}{\gamma + 1} (\nabla - \nabla_{\text{ad}}) \frac{\ell}{H_p} = \frac{1}{\beta} (\nabla - \nabla') \frac{\ell}{H_p}. \quad (\text{A42})$$

This equation can be derived from MLT, where $\beta = 2$ is usually adopted. Using equation (A42) in equation (A35) we have

$$\left(V_{c0}^r \right)^2 = \frac{1}{\beta \alpha} \left(1 - \frac{2}{3} Q \right) g H_p \frac{\chi_T}{\chi_\rho} (\nabla - \nabla') \left(\frac{\ell}{H_p} \right)^2, \quad (\text{A43})$$

where Q is defined as $k_r^2/k^2 = 2Q/3$ meaning $Q = 1$ for isotropic eddies ([Gabriel et al. 1975](#)). In MLT,

$$\frac{1}{\beta \alpha} \left(1 - \frac{2}{3} Q \right) = 1/8 \quad (\text{A44})$$

is often adopted (e.g. [Heney et al. 1965](#)), which corresponds to the relation

$$\alpha = \frac{8}{\beta} \left(1 - \frac{2}{3} Q \right). \quad (\text{A45})$$

Therefore, we can adopt $(Q, \alpha, \beta) = (1, 1.3, 2)$ as a standard set of parameters.

A4 Pulsational perturbation on convection

In this subsection we consider spherical symmetric (radial) linear Lagrangian perturbation δ for convective eddies which, as in the previous subsection, are treated locally. We will present δV^r and $\delta S'$ (convection variables perturbed by pulsation) as functions of regular pulsation variables.

A4.1 Thermal relations

Applying pulsational perturbations to equation (A29) and using equation (A36), we obtain

$$\Sigma_1 \frac{\delta S'}{S'} - K_{\text{rad}} \frac{\delta V^r}{V^r} = \left(\frac{\beta}{\tau} + K_{\text{rad}} \right) \frac{\delta(dS/dr)}{(dS/dr)} - i\sigma \left(1 - \frac{\chi_T}{\chi_\rho} \right) \frac{\delta S}{C_p} - \delta K_{\text{rad}} + \frac{\beta}{\tau} \left(\frac{\delta H_p}{H_p} \right), \quad (\text{A46})$$

where we defined

$$\Sigma_1 \equiv \left(i\sigma + \frac{\beta}{\tau} + \beta\sigma_r + K_{\text{rad}} \right) \quad (\text{A47})$$

A4.2 Mechanical relations

From the momentum equation (A18) of convective eddies, we obtain

$$\begin{aligned} \left(i\sigma + \frac{\alpha}{\tau} + \alpha\sigma_r\right)\delta\mathbf{V}_c &= \frac{\alpha}{\tau}\frac{\delta\tau}{\tau}\mathbf{V}_{c0} - i\sigma(\mathbf{V}_{c0} \cdot \nabla)\xi \\ &- ik\delta\left(\frac{P'}{\rho}\right) - \delta\left(\frac{\rho'}{\rho}\right)\nabla\psi - \frac{\rho'}{\rho}\delta(\nabla\psi). \end{aligned} \quad (\text{A48})$$

From equation (A19) we obtain

$$\mathbf{k} \cdot \delta\mathbf{V}_c = 0. \quad (\text{A49})$$

Taking the inner product between \mathbf{k} and equation (A48) and using equation (A49) we have

$$0 = -i\sigma\mathbf{k} \cdot [(\mathbf{V}_{c0} \cdot \nabla)\xi] - ik^2\delta\left(\frac{P'}{\rho}\right) - k_r\delta\left(\frac{\rho'}{\rho}\right)\frac{d\psi}{dr} - \frac{\rho'}{\rho}k_r\delta\left(\frac{d\psi}{dr}\right), \quad (\text{A50})$$

Substituting above equation into eq. (A48), we eliminate P' ,

$$\begin{aligned} \left(i\sigma + \frac{\alpha}{\tau} + \alpha\sigma_r\right)\delta\mathbf{V}_c &= i\sigma\left[\frac{\mathbf{k}}{k^2}\mathbf{k} \cdot (\mathbf{V}_{c0} \cdot \nabla)\xi - (\mathbf{V}_{c0} \cdot \nabla)\xi\right] \\ &- g\frac{\chi T}{\chi\rho}\left(\frac{k_r\mathbf{k}}{k^2} - \mathbf{e}_r\right)\frac{\delta S'}{C_p} + \frac{\alpha}{\tau}\left(\frac{\delta H_p}{H_p} - \frac{\delta v}{v}\right)\mathbf{V}_{c0} \\ &- \frac{\alpha V_{c0}^r}{\tau g}\frac{k^2}{k_h^2}\left[\frac{\mathbf{k}}{k^2}\mathbf{k} \cdot \delta(\nabla\psi) - \delta(\nabla\psi)\right], \end{aligned} \quad (\text{A51})$$

where we used the relations $\tau = \ell/v$ and $\ell \propto H_p$, and the relation between ρ' and S' (eq. A27).

The radial component of equation (A51) is can be written as

$$\begin{aligned} \Sigma_2\frac{\delta V_c^r}{V_c^r} - \frac{\alpha}{\tau}\frac{\delta S'}{S'} &= i\sigma\left[\frac{2Q}{3}\left(\frac{d\xi}{dr} - \frac{\xi}{r}\right) - \frac{d\xi}{dr}\right] \\ &+ \frac{\alpha}{\tau}\frac{\delta H_p}{H_p} + \frac{\alpha}{\tau g}\delta\left(\frac{d\psi}{dr}\right), \end{aligned} \quad (\text{A52})$$

where we defined

$$\Sigma_2 \equiv i\sigma + \frac{2\alpha}{\tau} + \alpha\sigma_r. \quad (\text{A53})$$

In deriving equation (A52), we assumed the relation $\delta v/v = \delta V_c^r/V_{c0}^r$, and used the relation between S'_0 and V_{c0}^r given in equation (A35). We also used the relation

$$\frac{k_r}{k^2}\mathbf{k} \cdot (\mathbf{V}_{c0} \cdot \nabla)\xi = \frac{2Q}{3}V_{c0}^r\left(\frac{d\xi}{dr} - \frac{\xi}{r}\right), \quad (\text{A54})$$

which can be derived from the relations $\mathbf{k} \cdot \mathbf{V}_{c0} = 0$ (eq. A33) and $k_r^2/k^2 = 2Q/3$ (eq. A43).

From equations (A46) and (A52) we can express $\delta V_c^r/V_c^r$ and $\delta S'/S'$ as functions of pulsation variables, which are used in equation (A61) (below) to obtain the Lagrangian perturbation of convective luminosity, δL_{conv} .

A5 Equations for linear radial pulsations

Using radial displacement ξ , the Lagrangian perturbations of pressure δP , and entropy δS , linearised momentum (A4) and mass conservation (A6) equations can be written as

$$r\frac{d}{dr}\left(\frac{\xi_r}{r}\right) = -3\frac{\xi_r}{r} - \frac{\delta\rho}{\rho} = -3\frac{\xi_r}{r} - \frac{1}{\Gamma_1}\frac{\delta p}{p} + \frac{\chi T}{\chi\rho}\frac{\delta S}{C_p} \quad (\text{A55})$$

and

$$\frac{d}{d\ln r}\left(\frac{\delta p}{p}\right) = V\left(\frac{\sigma^2 r}{g} + 4\right)\frac{\xi_r}{r} + V\frac{\delta p}{p}, \quad (\text{A56})$$

in which we have neglected turbulent pressure term $(\overline{\mathbf{V}_c \cdot \nabla \mathbf{V}_c})'_r$.

A5.1 Energy conservation

Linearized energy conservation may be written as

$$i\sigma T\delta S = \epsilon_n\left(\epsilon_\rho\frac{\delta\rho}{\rho} + \epsilon_T\frac{\delta T}{T}\right) - L_r\frac{d}{dM_r}\left(\frac{\delta L_r}{L_r}\right) - \left(\frac{\delta L_r}{L_r}\right)\frac{dL_r}{dM_r}, \quad (\text{A57})$$

where $\epsilon_\rho \equiv (\partial \ln \epsilon_n / \partial \ln \rho)_T$ and $\epsilon_T \equiv (\partial \ln \epsilon_n / \partial \ln T)_\rho$. Luminosity perturbation can be expressed as

$$\frac{\delta L_r}{L_r} = \frac{L_{\text{rad}}}{L_r}\frac{\delta L_{\text{rad}}}{L_{\text{rad}}} + \frac{L_{\text{con}}}{L_r}\frac{\delta L_{\text{con}}}{L_{\text{con}}}. \quad (\text{A58})$$

Radiative luminosity L_{rad} and it's Lagrangian perturbation δL_{rad} are given as

$$L_{\text{rad}} = -(4\pi r^2)^2\frac{4acT^4}{3\kappa}\frac{d\ln T}{dM_r}, \quad (\text{A59})$$

and

$$\frac{\delta L_{\text{rad}}}{L_{\text{rad}}} = 4\frac{\xi_r}{r} + 4\frac{\delta T}{T} - \frac{\delta\kappa}{\kappa} + \frac{1}{d\ln T/dM_r}\frac{d}{dM_r}\left(\frac{\delta T}{T}\right). \quad (\text{A60})$$

For the perturbation of convective luminosity we have from equation (A13)

$$\frac{\delta L_{\text{con}}}{L_{\text{con}}} = 2\frac{\xi_r}{r} + \frac{\delta F_{\text{con}}}{F_{\text{con}}} = 2\frac{\xi_r}{r} + \frac{\delta\rho}{\rho} + \frac{\delta T}{T} + \frac{\delta V^r}{V^r} + \frac{\delta S'}{S'}. \quad (\text{A61})$$

The convection variables $\delta V^r/V^r$ and $\delta S'/S'$ can be expressed by ordinary pulsation variables using equations (A46) and (A52).

A6 Summary of the linear differential equations for radial pulsations

We define non-dimensional variables $Z_1 \dots Z_4$ as

$$Z_1 = \frac{\delta P}{P}, \quad Z_2 = \frac{\delta S}{C_p}, \quad Z_3 = \frac{\delta r}{r}, \quad Z_4 = \frac{\delta L_r}{L_r}. \quad (\text{A62})$$

The differential equations may be given as

$$\begin{aligned} \frac{dZ_1}{d\ln r} &= VZ_1 + V(c_1\omega^2 + 4)Z_3, \\ \frac{dZ_2}{d\ln r} &= b_1Z_1 + b_2Z_2 + b_3Z_3 - b_4\frac{L_r}{L_{\text{rad}}}Z_4, \\ \frac{dZ_3}{d\ln r} &= -\frac{1}{\Gamma_1}Z_1 + \frac{\chi T}{\chi\rho}Z_2 - 3Z_3, \\ \frac{dZ_4}{d\ln r} &= b_5Z_1 + b_6Z_2 - \frac{d\ln L_r}{d\ln r}Z_4, \end{aligned} \quad (\text{A63})$$

where $V \equiv -d\ln P/d\ln r$, $c_1 \equiv (r/R)^3 M/M_r$, and the pulsation angular frequency σ is normalized as $\omega = \sigma\sqrt{\frac{R^3}{GM}}$. Coefficients

$b_1 \dots b_6$ are defined as

$$b_1 = b_4 \left[(4 - \kappa_T) \nabla_{\text{ad}} - \frac{\kappa_\rho}{\Gamma_1} + \frac{\nabla_{\text{ad}}}{\nabla} \left(\frac{d \ln \nabla_{\text{ad}}}{d \ln P} - 1 \right) + f_{\text{CR}} \left(\nabla_{\text{ad}} + \frac{1}{\Gamma_1} + a_p \right) \right],$$

$$b_2 = b_4 \left[4 - \kappa_T + \kappa_\rho \frac{\chi_T}{\chi_\rho} + f_{\text{CR}} \left(1 - \frac{\chi_T}{\chi_\rho} + a_s \right) \right],$$

$$b_3 = b_4 \left[4 - \frac{\nabla_{\text{ad}}}{\nabla} (c_1 \omega^2 + 4) + 2 f_{\text{CR}} (1 + a_r) \right],$$

$$b_4 = \left[\frac{1}{V \nabla} + \frac{f_{\text{CR}} \Sigma_{23}}{\Sigma_4} \frac{K_{\text{rad}} + \beta / \tau}{V (\nabla - \nabla_{\text{ad}})} \right]^{-1},$$

$$b_5 = \frac{4\pi r^3 \rho \epsilon}{L_r} \left(\epsilon_T \nabla_{\text{ad}} + \frac{\epsilon_\rho}{\Gamma_1} \right),$$

$$b_6 = \frac{4\pi r^3 \rho \epsilon}{L_r} \left(\epsilon_T - \epsilon_\rho \frac{\chi_T}{\chi_\rho} \right) - i\omega \sqrt{\frac{GM}{R^3}} \frac{4\pi r^3 T C_p}{L_r},$$

where $f_{\text{CR}} \equiv L_{\text{conv}}(r) / L_{\text{rad}}(r)$,

$$a_r = \frac{1}{\Sigma_4} \left[i\sigma \Sigma_5 v_{rr} + \Sigma_{23} \left(3K_{\text{rad}} + \frac{\beta}{\tau} \right) + \frac{1}{\tau} (\alpha \Sigma_5 + \beta \Sigma_{23}) \right],$$

$$a_p = \frac{1}{\Sigma_4} \left[i\sigma \Sigma_5 \frac{v_{r\rho}}{\Gamma_1} + \Sigma_{23} s_p + \frac{1}{\tau} (\alpha \Sigma_5 + \beta \Sigma_{23}) \left(1 - \frac{1}{\Gamma_1} \right) \right],$$

$$a_s = \frac{1}{\Sigma_4} \left[-i\sigma \Sigma_5 v_{r\rho} \frac{\chi_T}{\chi_\rho} + \Sigma_{23} s_s + \frac{1}{\tau} (\alpha \Sigma_5 + \beta \Sigma_{23}) \frac{\chi_T}{\chi_\rho} \right],$$

$$\Sigma_{23} \equiv \Sigma_2 + \frac{\alpha}{\tau}, \quad \Sigma_4 \equiv \Sigma_1 \Sigma_2 - K_{\text{rad}} \frac{\alpha}{\tau}, \quad \Sigma_5 \equiv \Sigma_1 + K_{\text{rad}},$$

$$v_{rr} \equiv 1 - Q - \frac{\alpha}{i\sigma\tau}, \quad v_{r\rho} \equiv 1 - \frac{2Q}{3},$$

$$s_p \equiv \frac{1}{\Gamma_1} \left(K_{\text{rad}} + \frac{\beta}{\tau} \right) - K_{\text{rad}} \left[(3 - \kappa_T) \nabla_{\text{ad}} - 2 - \frac{\kappa_\rho}{\Gamma_1} \right],$$

$$s_s \equiv - \left(K_{\text{rad}} + \frac{\beta}{\tau} \right) \left[\frac{\chi_T}{\chi_\rho} - \frac{d \ln C_p / d \ln p}{\nabla - \nabla_{\text{ad}}} \right] + \left[i\sigma \left(\frac{\chi_T}{\chi_\rho} - 1 \right) - K_{\text{rad}} \left(3 - \kappa_T + \kappa_\rho \frac{\chi_T}{\chi_\rho} \right) \right].$$

This paper has been typeset from a $\text{\TeX}/\text{\LaTeX}$ file prepared by the author.